Science

AAAS

Revealing Magnetic Interactions from Single-Atom Magnetization Curves

structure of a group II intron from an ancient lineage is therefore notable because it may represent a glimpse of the primordial catalyst that triggered the evolution of diverse life forms on Earth.

References and Notes

1. A. M. Pyle, A. M. Lambowitz, *The RNA World* (Cold Spring Harbor Laboratory Press, Cold Spring Harbor, NY, ed. 3, 2006).
2. S. Zimmerly, H. Guo, P. Perlman, A. Lambowitz, *Cell* **82**, 545 (1995).
3. A. Robart, W. Seo, S. Zimmerly, *Proc. Natl. Acad. Sci. U.S.A.* **104**, 6620 (2007).
4. J. Ferat, F. Michel, *Nature* **364**, 358 (1993).
5. Y. Vallès, K. Halanych, J. Boore, *PLoS ONE* **3**, e1488 (2008).
6. P. Sharp, *Science* **254**, 663 (1991).
7. T. Cech, *Cell* **44**, 207 (1986).
8. A. Jacquier, F. Michel, *Cell* **50**, 17 (1987).
9. M. Costa, F. Michel, E. Westhof, *EMBO J.* **19**, 5007 (2000).
10. O. Fedorova, T. Mitros, A. Pyle, *J. Mol. Biol.* **330**, 197 (2003).
11. S. Mikheeva, H. Murray, H. Zhou, B. Turczyk, K. Jarrell, *RNA* **6**, 1509 (2007).
12. A. de Lencastre, A. Pyle, *RNA* **14**, 11 (2007).
13. H. Wank, J. SanFilippo, R. Singh, M. Matsuura, A. Lambowitz, *Mol. Cell* **4**, 239 (1999).
14. U. Schmidt, M. Podar, U. Stahl, P. Perlman, *RNA* **2**, 1161 (1996).
15. S. Boulanger *et al.*, *Mol. Cell. Biol.* **15**, 4479 (1995).
16. A. de Lencastre, S. Hamill, A. Pyle, *Nat. Struct. Mol. Biol.* **12**, 626 (2005).
17. N. Toor, G. Hausner, S. Zimmerly, *RNA* **7**, 1142 (2001).
18. N. Toor, A. Robart, J. Christianson, S. Zimmerly, *Nucleic Acids Res.* **34**, 6461 (2006).
19. J. Rest, D. Mindell, *Mol. Biol. Evol.* **20**, 1134 (2003).
20. M. Podar, V. Chu, A. Pyle, P. Perlman, *Nature* **391**, 915 (1998).
21. M. Granlund, F. Michel, M. Norgren, *J. Bacteriol.* **183**, 2560 (2001).
22. Materials and methods are available as supporting material on *Science* Online.
23. W. Hendrickson, J. Smith, S. Sheriff, *Methods Enzymol.* **115**, 41 (1985).
24. A. Keel, R. Rambo, R. Batey, J. Kieft, *Structure* **15**, 761 (2007).
25. C. Harris-Kerr, M. Zhang, C. Peebles, *Proc. Natl. Acad. Sci. U.S.A.* **90**, 10658 (1993).
26. A. Jacquier, F. Michel, *J. Mol. Biol.* **213**, 437 (1990).
27. M. Boudvillain, A. de Lencastre, A. Pyle, *Nature* **406**, 315 (2000).
28. M. Costa, E. Déme, A. Jacquier, F. Michel, *J. Mol. Biol.* **267**, 520 (1997).
29. M. Boudvillain, A. Pyle, *EMBO J.* **17**, 7091 (1998).
30. M. Costa, F. Michel, *EMBO J.* **14**, 1276 (1995).
31. O. Fedorova, A. Pyle, *EMBO J.* **24**, 3906 (2005).
32. A. Pyle, O. Fedorova, C. Waldsich, *Trends Biochem. Sci.* **32**, 138 (2007).
33. M. Tamura, S. Holbrook, *J. Mol. Biol.* **320**, 455 (2002).
34. P. Adams, M. Stahley, A. Kosek, J. Wang, S. Strobel, *Nature* **430**, 45 (2004).
35. M. Podar *et al.*, *RNA* **4**, 151 (1998).
36. R. Sigel *et al.*, *Nat. Struct. Mol. Biol.* **11**, 187 (2004).
37. L. Zhang, J. Doudna, *Science* **295**, 2084 (2002).
38. G. Chanfreau, A. Jacquier, *Science* **266**, 1383 (1994).
39. P. Gordon, J. Piccirilli, *Nat. Struct. Biol.* **8**, 893 (2001).
40. T. Steitz, J. Steitz, *Proc. Natl. Acad. Sci. U.S.A.* **90**, 6498 (1993).
41. M. Stahley, S. Strobel, *Science* **309**, 1587 (2005).
42. K. Baeyens, H. De Bondt, A. Pardi, S. Holbrook, *Proc. Natl. Acad. Sci. U.S.A.* **93**, 12851 (1996).
43. N. Leontis, E. Westhof, *RNA* **7**, 499 (2001).
44. M. Podar, S. Dib-Hajj, P. Perlman, *RNA* **1**, 828 (1995).
45. M. Podar, P. Perlman, *RNA* **5**, 318 (1999).
46. P. Gordon, R. Fong, J. Piccirilli, *Chem. Biol.* **14**, 607 (2007).
47. G. Shukla, R. Padgett, *Mol. Cell* **9**, 1145 (2002).
48. S. Yean, G. Wuenschell, J. Termini, R. Lin, *Nature* **408**, 881 (2000).
49. H. Madhani, C. Guthrie, *Genes Dev.* **8**, 1071 (1994).
50. W. Martin, E. Koonin, *Nature* **440**, 41 (2006).
51. www.pymol.org
52. We thank K. Rajashankar, N. Sukumar, and I. Kourinov of Northeastern Collaborative Access Team (NE-CAT) beamline ID-24 at the Advanced Photon Source (APS) of Argonne National Laboratory. We also thank J. Osipiuk and the staff at Structural Biology Center Collaborative Access Team (SBC-CAT) beamline ID-19 at APS, and C. Whalen, A. Héroux, A. Saxena, W. Shi, and H. Robinson at X25 and X29 at the National Synchrotron Light Source at Brookhaven National Laboratory. We thank J. Cochrane, M. Stahley, and P. S. Perlman for their advice and support. We thank S. A. Strobel, M. Stahley, J. Cochrane, J. Cabral, J. Li-Pook-Than, O. Fedorova, and G. P. Wagner for comments on the manuscript, R. Batey for the gift of iridium hexamine, and H. Takami for the *O. iheyensis* strain. K.S.K. was supported by NIH training grant T15 LM07056. S.D.T. was supported by the U.S. Department of Defense through the National Defense Science and Engineering Graduate Fellowship Program and by a NSF Graduate Research Fellowship. This work was supported by the Howard Hughes Medical Institute (HHMI) and NIH grant GM50313 to A.M.P., who is an investigator of the HHMI. Coordinates, structure factors, and experimental phases of the group II intron have been deposited in the Protein Data Bank (accession number 3BWP, www.pdb.org) and the Nucleic Acid Database (accession number UR0130, http://ndbserver.rutgers.edu).

REPORTS

Revealing Magnetic Interactions from Single-Atom Magnetization Curves

Focko Meier,* Lihui Zhou, Jens Wiebe,† Roland Wiesendanger

The miniaturization of magnetic devices toward the limit of single atoms calls for appropriate tools to study their magnetic properties. We demonstrate the ability to measure magnetization curves of individual magnetic atoms adsorbed on a nonmagnetic metallic substrate with use of a scanning tunneling microscope with a spin-polarized tip. We can map out low-energy magnetic interactions on the atomic scale as evidenced by the oscillating indirect exchange between a Co adatom and a nanowire on Pt(111). These results are important for the understanding of variations that are found in the magnetic properties of apparently identical adatoms because of different local environments.

Magnetic nanostructures consisting of a few atoms on nonmagnetic substrates (adatoms) are explored as model systems for miniaturized data storage and spintronic devices and for the implementation of quantum computing. Because these structures are well defined and controllable on the atomic scale, they are ideally suited to study the fundamentals of magnetic interactions that are the ingredients of today's and future memory and computation technology.

Since the early days of modern research in magnetism, the magnetization in response to an external magnetic field (a magnetization curve) has been recorded to gather information on the basic properties of magnetic samples (*1*). Such curves can be used to deduce the sample's mag-

netic moment and magnetic anisotropy energy. The downscaling of samples from bulk over thin films and nanowires to nanodots requires an ever-increasing sensitivity of this method. It has been demonstrated that x-ray absorption spectroscopy with polarization analysis is able to measure magnetization curves of adatoms on a nonmagnetic substrate, albeit limited to large ensembles (*2*). Different approaches are potentially able to detect individual spins with nanometer spatial resolution ranging from magnetic resonance measurements (*3*) over magnetic exchange force microscopy (*4*) to scanning tunneling microscopy and spectroscopy (STM and STS) (*5–10*). Spin-averaged STS has been used to indirectly deduce the properties of single and coupled spins via the Kondo effect (*5*), the detection of noise (*6*, *7*), or the observation of exchange splittings (*8*, *9*). Inelastic electron tunneling has been adopted to measure the magnetic moments and anisotropy of individual atoms by spin-flip spectroscopy (*10*). This approach is complementary to the detection of magnetization curves but does not provide information on the dynamics of the spin and is so far restricted to adatoms on insulating layers. The method of choice for various substrates, spin-polarized STS (SP-STS), has been proven to detect single spins stabilized by direct exchange to

Institute of Applied Physics and Microstructure Research Center, University of Hamburg, Jungiusstrasse 11, D-20355 Hamburg, Germany.

*Present address: Laboratory of Atomic and Solid State Physics, Department of Physics, Cornell University, Ithaca, NY 14853, USA.

†To whom correspondence should be addressed. E-mail: jwiebe@physnet.uni-hamburg.de

(anti)ferromagnetic layers (*11*, *12*). However, the important step to individual spins in a nonmagnetic surrounding has been lacking because of the experimental challenge posed by spin instability.

We demonstrate the direct detection of the magnetization of single adatoms on a nonmagnetic metallic substrate as a function of an external magnetic field by SP-STS. Cobalt adatoms were used on a strongly polarizable platinum(111) substrate, forming large effective magnetic moments of about 5 Bohr magnetons (μ_B) with a strong out-of-plane anisotropy (*2*). Our intent is to measure the magnetic interaction between stripes of one atomic layer Co grown at room temperature (*13*) and the individual Co adatoms deposited at about 25 K on the bare Pt(111) (Fig. 1) (*14*, *15*). The monolayer (ML) stripes, which have a magnetization, $\vec{M}_{ML}$, perpendicular to the surface (*13*), serve as the calibration standard for the magnetic properties of the SP-STM tip. When we use out-of-plane-oriented tips, the up and down domains exhibit a different spin-resolved dI/dV signal as seen in Fig. 1. It is then possible to characterize the spin polarization and magnetization, $\vec{M}_T$, of the foremost tip atom acting as a detector for the magnetization of the adatom, $\vec{M}_A$ (fig. S1). The dI/dV signal recorded above a particular adatom is sensitive to the relative orientation of $\vec{M}_T$ and $\vec{M}_A$ (*16*),

$$\mathrm{d}I/\mathrm{d}V \propto (\mathrm{d}I/\mathrm{d}V)_0 + (\mathrm{d}I/\mathrm{d}V)_{SP}\, \vec{M}_T \cdot \vec{M}_A \quad (1)$$

where the first term and the second term represent the bias-voltage-dependent spin-averaged and spin-resolved parts of dI/dV, respectively. The dI/dV signal is averaged over about 10 ms. dI/dV as a function of an external magnetic field, $\vec{B}$, is thus a direct measure for the component of the time-averaged magnetization $\langle \vec{M}_A \rangle$ in the out-of-plane direction.

Before analyzing the $\vec{B}$-dependent magnetization of single adatoms, their exact location with respect to the underlying substrate has to be determined. The Co adatoms can sit on either hexagonal close-packed (hcp) or face-centered cubic (fcc) lattice sites, which are unambiguously distinguishable by their dI/dV at small negative bias voltages (Fig. 2A inset and fig. S2). In the dI/dV curves, the fcc adatoms show a characteristic peak at about −0.05 V below the Fermi level E_F (V = 0 V), which is shifted slightly downward for hcp adatoms. When $\vec{B}$ is reversed from −0.3 T to +0.3 T, this peak strongly changes intensity because of the alignment of $\langle \vec{M}_A \rangle$ with $\vec{B}$, leading to parallel and antiparallel orientation of $\langle \vec{M}_A \rangle$ and $\vec{M}_T$ ($\vec{M}_T$ is constant as shown in fig. S1). Similar intensity changes can be observed in nearly the entire voltage range and can be quantified by the magnetic asymmetry $A_{magn} = (\mathrm{d}I/\mathrm{d}V_p - \mathrm{d}I/\mathrm{d}V_{ap})/(\mathrm{d}I/\mathrm{d}V_p + \mathrm{d}I/\mathrm{d}V_{ap})$, where d$I$/d$V_p$ and dI/dV_{ap} are the curves for parallel and antiparallel orientation, respectively (Fig. 2B). The strongest asymmetry occurs at the energy of the prominent peak below E_F, proving that this adatom state is strongly spin-polarized. Because this state is sensitive to the
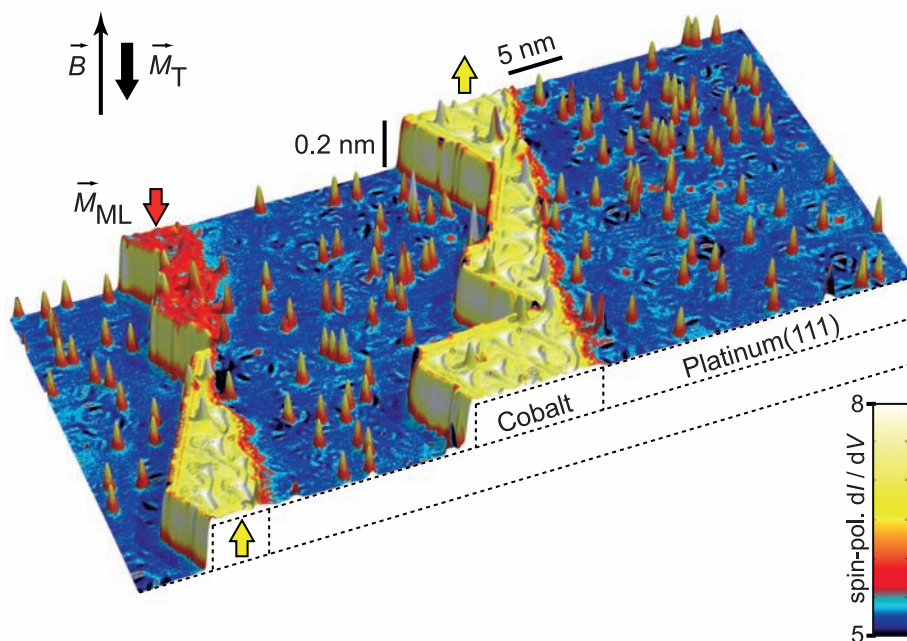

Fig. 1. Overview of the sample of individual Co adatoms on the Pt(111) surface (blue) and Co ML stripes (red and yellow) attached to the step edges (STM topograph colorized with the simultaneously recorded spin-polarized dI/dV map measured with an STM tip magnetized antiparallel to the surface normal). An external $\vec{B}$ can be applied perpendicular to the sample surface in order to change the magnetization of adatoms $\vec{M}_A$, ML stripes $\vec{M}_{ML}$, or tip $\vec{M}_T$. The ML appears red when $\vec{M}_{ML}$ is parallel to $\vec{M}_T$ and yellow when $\vec{M}_{ML}$ is antiparallel to $\vec{M}_T$. (Tunneling parameters are as follows: I = 0.8 nA, V = 0.3 V, modulation voltage V_{mod} = 20 mV, T = 0.3 K.)

Fig. 2. Spin-polarized dI/dV curves from individual Co adatoms. (**A**) Curves measured on an hcp and on an fcc adatom by using the same tip as in fig. S1 with $\vec{B}$ as indicated (averages from six single curves, fcc curves are offset for clarity). The time-averaged magnetization of the adatoms $\langle \vec{M}_A \rangle$ is aligned with $\vec{B}$, resulting in a change in the dI/dV curve depending on the relative orientation of $\langle \vec{M}_A \rangle$ and $\vec{M}_T$ as indicated. a.u., arbitrary units. (Inset) Topograph colorized with simultaneously recorded dI/dV map at V_{stab} = −0.1 V of an area with two hcp (orange) and two fcc (blue) adatoms. (**B**) Magnetic asymmetry (A_{magn}) calculated from the curves of (A). (Tunneling parameters are as follows: I_{stab} = 1 nA, V_{stab} = 0.6 V, V_{mod} = 10 mV, T = 0.3 K.)
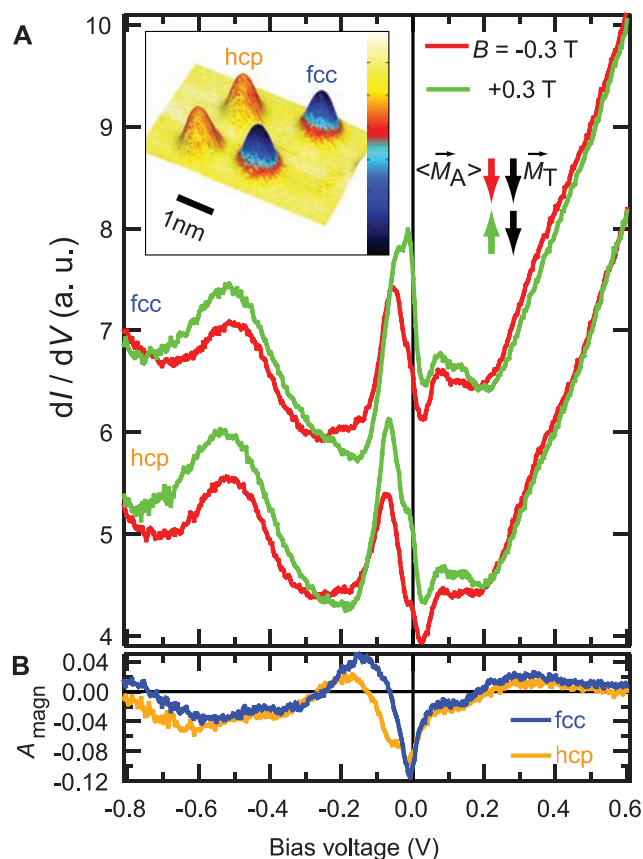
Fig. 3. (**A** and **B**) Topographs of an area with several adatoms colorized with the spin-polarized dI/dV map at $B = -0.5$ T parallel to the tip magnetization $\vec{M}_\mathrm{T}$ (A) and $B = +0.5$ T antiparallel to $\vec{M}_\mathrm{T}$ (B) ($T = 0.3$ K). (**C**) Magnetization curves from the same adatom taken at different temperatures as indicated (dots). Reversal of $\vec{M}_\mathrm{T}$ is corrected (fig. S3). The solid lines are fits to the data (see text). The insets show the resulting histograms of the fitted magnetic moments (in μ_B) for the same 11 adatoms at $T = 4.2$ K (black) and at 0.3 K (red) (top histogram) and for 38 hcp (orange) and 46 fcc (blue) adatoms at 0.3 K (bottom histogram, fcc bars stacked on hcp). (**D**) Magnetization curves of four adatoms at 0.3 K with fit curves and resulting B_sat of 99% saturation. The inset shows the histogram of B_sat (in T) for the same adatoms used in the lower histogram in (C) (fcc bars stacked on hcp). [Curves in (C) and (D) are offset for clarity. Tunneling parameters are as follows: $I = 0.8$ nA, $V = 0.3$ V, $V_\mathrm{mod} = 20$ mV.]
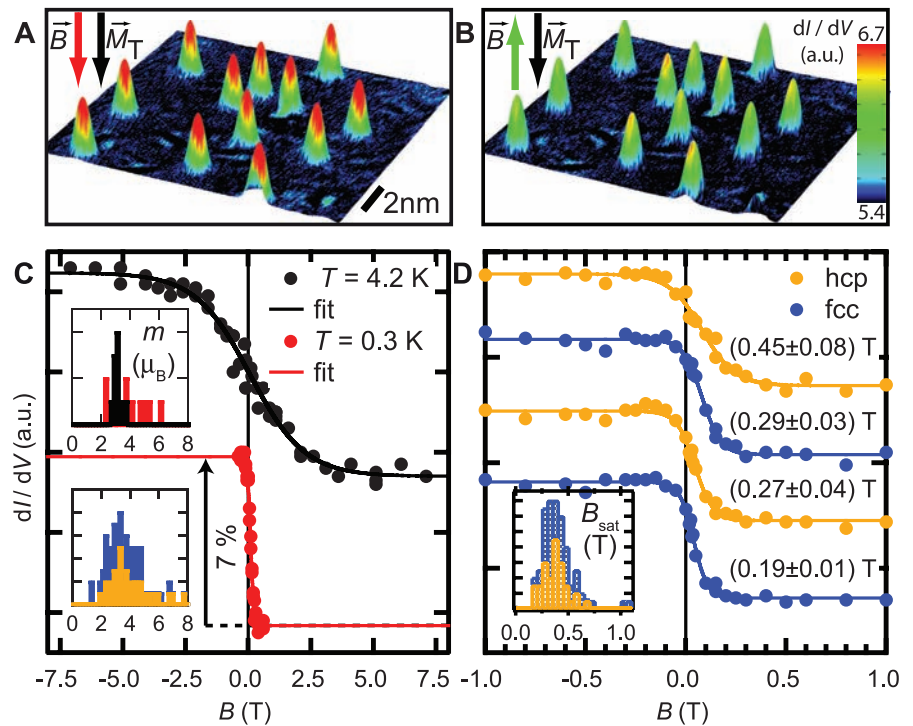
lattice site of the adatom and to its spin orientation, it is not suited to separate structural and magnetic contributions. Instead, the dI/dV signal at +0.3 V has a small but sufficient asymmetry with negligible influence of the lattice site and will be used to record $\langle \vec{M}_\mathrm{A} \rangle$ as a function of $\vec{B}$.

Focusing first on isolated adatoms [mean nearest neighbor distance of 2.4 ± 1 nm (SEM)] that are more than 8 nm distant from the ML, Fig. 3, A and B, shows dI/dV maps recorded at -0.5 T and $+0.5$ T. As in the dI/dV curves, the dI/dV signal on the adatoms is reduced for antiparallel configuration of $\langle \vec{M}_\mathrm{A} \rangle$ and $\vec{M}_\mathrm{T}$. Similar dI/dV maps have been recorded at different $\vec{B}$, which was varied in small steps from -7.5 T to $+7.5$ T and back to -7.5 T. The dI/dV signal was averaged above individual adatoms (about 0.25 nm^2) and plotted as a function of $\vec{B}$ (Fig. 3C). The magnetization curves are shifted slightly to the right because of the residual stray field of the tip, $\vec{B}_\mathrm{T}$ (fig. S3A).

We observed S-shaped curves for both temperatures but with strongly different saturation fields, $B_\mathrm{sat} \approx 5$ T ($T = 4.2$ K) and $B_\mathrm{sat} \approx 0.3$ T ($T = 0.3$ K). No signs of hysteresis are observed; that is, $\vec{M}_\mathrm{A}$ behaves paramagnetically and statistically switches between up and down with a rate much faster than the current time resolution of the experiment (>100 Hz). It has been reported that Co adatoms on Pt(111) have a large out-of-plane magnetocrystalline anisotropy of $K = 9.3$ meV per atom (at 5.5 K), corresponding to an energy barrier between up- and downward pointing $\vec{M}_\mathrm{A}$ of about 100 K (2). Because our lowest temperature is 350 times smaller, we can exclude thermally induced switching of $\vec{M}_\mathrm{A}$ across such a barrier (17). Thus, if the description in (2) is correct, our results imply the dominance of a temperature-independent

switching process, for example, quantum tunneling of the magnetization or current-induced magnetization switching by inelastic processes.

In order to gain information on the magnetic moment, m, we fitted the measured magnetization curves. It is interesting to evaluate whether a quasi-classical description is appropriate (2) because the magnetization is that of an individual atom averaged over a time window without ensemble averaging. We thus calculate M_A by using a magnetic energy function $E(\theta,B) = -m(B - B_\mathrm{T})\cos\theta - K(\cos\theta)^2$, where θ is the angle between the magnetic moment and $\vec{B}$. We numerically fit the magnetization curves by variation of m, of the saturation magnetization, M_sat, and of the tip stray field, B_T. Because of the lack of a hard axis magnetization curve, K is not an appropriate independent fit parameter. Therefore, a fixed value $K = 9.3$ meV is taken (2). The corresponding fit curves in Fig. 3C excellently reproduce the single-atom magnetization curves. Probably a strong hybridization of the adatom states with the Pt bands leads to a quasi-classical behavior of the total magnetic moment (2, 18).

Similar magnetization curves as in Fig. 3C have been recorded by using several tips for about 80 different adatoms showing qualitatively the same paramagnetic shape. The insets contain the histograms of the fitted m. Surprisingly, the variance in m for the same adatoms increases notably at $T = 0.3$ K. The bottom histogram indicates a broad distribution from about 2μ_B to 6μ_B with arithmetic means of $m_\mathrm{hcp} = (3.9 \pm 0.2)\mu_\mathrm{B}$ and $m_\mathrm{fcc} = (3.5 \pm 0.2)\mu_\mathrm{B}$. These are larger than the 4.2 K values [$m_\mathrm{hcp} = (3.0 \pm 0.3)\mu_\mathrm{B}$ and $m_\mathrm{fcc} = (3.1 \pm 0.1)\mu_\mathrm{B}$] (19). Figure 3D shows the measured magnetization curves and the correspond-

ing fits of four different adatoms where the variance in m is visible as a spreading in the saturation fields B_sat.

Because the peculiar spreading in the fitted m is obtained similarly for hcp and fcc adatoms, we can exclude an adsorption-site-induced variance in the magnetic moment. Another reason for variance can be electronic substrate inhomogeneity because of the subsurface-defect scattering seen in Fig. 1 (20). However, this is very unlikely: (i) There is no obvious correlation between m and the scattering-state distribution; (ii) the variance in m is strongly increased for lower temperature, whereas the scattering states remain unaffected. Thus, we propose that the variation in m is induced by a magnetic interaction between the adatoms with an energy scale of about $k_\mathrm{B} \cdot 0.3$ K = 25 µeV. From the spreading of B_sat found in the histogram in Fig. 3D (0.2 T to 0.7 T), we get a rough estimate for the interaction strength $J = m \cdot (0.7\ \mathrm{T} - 0.2\ \mathrm{T})/2 \approx 50$ µeV ($m = 3.7\mu_\mathrm{B}$). This is consistent with an increased variance only at very low temperatures. Direct exchange and dipolar interactions can be neglected because of the large separation of the adatoms. Therefore, we assume that indirect exchange via the Pt substrate is responsible for the variance.

If this hypothesis is true, a long-range coupling between the adatoms and the ML is expected. Focusing on adatoms close to the right of the ML, Fig. 4A shows the magnetization curve of a particular ML stripe and of an adatom with a distance of $d \approx 1.5$ nm. The ML shows a regular squarelike hysteresis corresponding to ferromagnetic behavior. In the down sweep (blue curve), its magnetization switches from up (high signal) to down (low signal) at $B = -0.5$ T, and in the up sweep (red curve) it switches from down to up at

Fig. 4. Magnetic exchange between adatoms and ML stripe. (**A** to **C**) Magnetization curves measured on the ML (straight lines) and on the three adatoms (dots) A, B, and C visible in the inset topograph of (**D**). The blue color indicates the down sweep from B = +1 T to −1 T (and red, the up sweep from −1 T to +1 T) (dI/dV signal on ML inverted for clarity). The vertical arrows indicate the exchange bias field, B_{ex}, which is converted into the exchange energy (using m = 3.7μ_B) for the corresponding magenta points in the plot (**D**). (Tunneling parameters are as follows: I = 0.8 nA, V = 0.3 V, V_{mod} = 20 mV, T = 0.3 K.) (**D**) Dots show measured exchange energy as a function of distance from ML as indicated by the arrow in the inset (about 50° to [11$\bar{2}$]). The black line is the dipolar interaction calculated from the stray field of a 10-nm-wide stripe with saturation magnetization 1.3 × 10⁶ A/m. The red, blue, and green lines are fits to 1D, 2D, and 3D range functions for indirect exchange. Horizontal error bars are due to the roughness of the Co-ML-stripe edge, whereas the vertical ones are due to the uncertainty in B_{ex}.
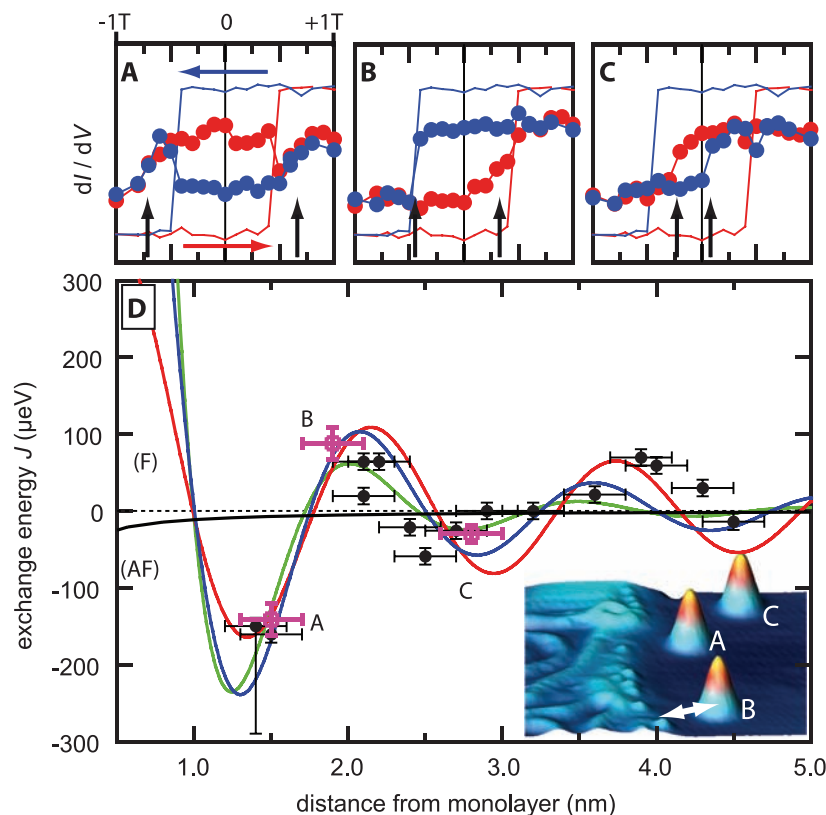
+0.5 T. The adatom behaves completely different than the previously described distant ones. In the down sweep, its magnetization switches from up to down already at large positive B = +0.7 T (see arrow). It then switches back to up simultaneously with the reversal of the stripe at −0.5 T. Only at −0.7 T is the adatom magnetization again forced into the down state (see arrow). The same behavior is observed for the up sweep but now with the stripe magnetization pointing downward and the adatom magnetization pointing upward at zero field. The adatom feels an antiferromagnetic (AF) coupling to the stripe, which is broken by an exchange bias of B_{ex} = ± 0.7 T corresponding to an interaction energy of J = $-m \cdot B_{ex} \approx$ −150 μeV (m = 3.7 μ_B). The magnetization curve of a more distant adatom shows a ferromagnetic (F) coupling (Fig. 4B); that is, the adatom magnetization is forced parallel to the stripe at zero field (J > 0). An even more distant adatom (Fig. 4C) again is antiferromagnetically coupled but with a lower B_{ex} smaller than the stripe coercivity (see arrows).

The interaction energies $J(d)$ determined from similar magnetization curves of many adatoms are plotted in Fig. 4D. A damped oscillatory behavior, which is reminiscent of Ruderman-Kittel-Kasuya-Yosida (RKKY)–like exchange, is observed (21–23). Note that dipolar coupling (black line) is always AF and negligible. Therefore, we conclude that the interaction is due to indirect exchange via the Pt electrons. In order to test whether an RKKY description is appropriate, Fig. 4D shows corresponding fits

to the data points using range functions $J(d)$ = $J_0 \cdot \cos(2 \cdot k_F \cdot d)/(2 \cdot k_F \cdot d)^D$ with different assumed dimensionalities, D (24, 25). A good agreement is found for D = 1 and a wavelength of λ_F = $2\pi/k_F \approx$ 3 nm, corresponding to an oscillation period of the exchange energy of 1.5 nm.

A dimensionality below 2 is indeed expected if the interaction is dominated by surface-related [two-dimensional (2D)] states and the superposition of the contributions from all Co atoms along the stripe edge attenuates the decay. This conclusion is analogous to the case of the exchange interaction between ferromagnetic layers separated by nonmagnetic metallic spacer layers, where the dominating states are bulk (3D) states, and the summation over the atoms in the layer can result in a 2D asymptotic behavior (26). Furthermore, the period of the measured oscillation leads to a λ_F that is a factor of 2 to 6 larger than typical Fermi wavelengths of the Pt(111) surface (20). We anticipate that effects similar to those found in layered systems explaining the long-period oscillation (26) also play a crucial role in the stripe-adatom interaction.

Our method not only reveals the magnetization of individual adatoms but also detects magnetic interactions with atomic resolution at an energy scale of 10 μeV. An increase in the time resolution should allow for the investigation of the dynamics in single and coupled spin systems (27). Together with the STM's ability to assemble nanometer-sized objects adatom by adatom, our method may be suitable for the fabrication and investigation of magnetic nanostructures on vari-

ous substrates as metallic, semiconducting (9), or thin insulating layers (10).

References and Notes

1. See, for example, S. Chikazumi, *Physics of Magnetism* (Wiley, New York, 1964).
2. P. Gambardella *et al.*, *Science* **300**, 1130 (2003).
3. D. Rugar, R. Budakian, H. J. Mamin, B. W. Chui, *Nature* **430**, 329 (2004).
4. U. Kaiser, A. Schwarz, R. Wiesendanger, *Nature* **446**, 522 (2007).
5. P. Wahl *et al.*, *Phys. Rev. Lett.* **98**, 056601 (2007).
6. Y. Manassen, R. J. Hamers, J. E. Demuth, A. Castellano, *Phys. Rev. Lett.* **62**, 2531 (1989).
7. C. Durkan, M. E. Welland, *Appl. Phys. Lett.* **80**, 458 (2002).
8. H. J. Lee, W. Ho, M. Persson, *Phys. Rev. Lett.* **92**, 186802 (2004).
9. D. Kitchen, A. Richardella, J.-M. Tang, M. E. Flatté, A. Yazdani, *Nature* **442**, 436 (2006).
10. C. F. Hirjibehedin *et al.*, *Science* **317**, 1199 (2007).
11. S. Heinze *et al.*, *Science* **288**, 1805 (2000).
12. Y. Yayon, V. W. Brar, L. Senapati, S. C. Erwin, M. F. Crommie, *Phys. Rev. Lett.* **99**, 067202 (2007).
13. F. Meier *et al.*, *Phys. Rev. B* **74**, 195411 (2006).
14. J. Wiebe *et al.*, *Rev. Sci. Instrum.* **75**, 4871 (2004).
15. Materials and methods are available as supporting material on *Science* Online.
16. D. Wortmann, S. Heinze, P. Kurz, G. Bihlmayer, S. Blügel, *Phys. Rev. Lett.* **86**, 4132 (2001).
17. R. L. White, *J. Magn. Magn. Mater.* **209**, 1 (2000).
18. However, a quantum mechanical two-level model with Zeeman splitting and off diagonal elements ±Γ that couple the spin up and down configurations was also tried to fit the data. It gives identical results as long as Γ << $k_B T$, corresponding to a reasonable switching rate Ω = Γ/$\hbar$ << 10¹⁰ Hz.
19. It has been checked that a variation of K in reasonable constraints 1 meV < K < 20 meV will not change the fitted m at T = 0.3 K because this temperature is too low to turn the magnetization considerably into hard axis direction. For the fits at T = 4.2 K, we would have to

assume $K \approx 1$ meV in order to reproduce the value of m given in (2).
20. J. Wiebe et al., Phys. Rev. B **72**, 193406 (2005).
21. M. A. Ruderman, C. Kittel, Phys. Rev. **96**, 99 (1954).
22. T. Kasuya, Prog. Theor. Phys. **16**, 45 (1956).
23. K. Yosida, Phys. Rev. **106**, 893 (1957).
24. B. Fischer, M. W. Klein, Phys. Rev. B **11**, 2025 (1975).
25. Y. Yafet, Phys. Rev. B **37**, 3948 (1986).
26. P. Bruno, C. Chappert, Phys. Rev. B **46**, 261 (1992).
27. S. Krause, L. Berbil-Bautista, G. Herzog, M. Bode, R. Wiesendanger, Science **317**, 1537 (2007).
28. Financial support from the Deutsche Forschungsgemeinschaft (SFB668, SFB508, and GrK1286) is gratefully acknowledged. We thank M. Bode, S. Heinze, E. Vedmedenko, A. Lichtenstein, S. Blügel, S. Lounis, and A. Schwarz for fruitful discussions and F. Marczinowski for assistance in illustration arts.

The Roles of Subsurface Carbon and Hydrogen in Palladium-Catalyzed Alkyne Hydrogenation

Detre Teschner,[1]* János Borsodi,[1,2] Attila Wootsch,[2] Zsolt Révay,[2] Michael Hävecker,[1] Axel Knop-Gericke,[1] S. David Jackson,[3] Robert Schlögl[1]

Alkynes can be selectively hydrogenated into alkenes on solid palladium catalysts. This process requires a strong modification of the near-surface region of palladium, in which carbon (from fragmented feed molecules) occupies interstitial lattice sites. In situ x-ray photoelectron spectroscopic measurements under reaction conditions indicated that much less carbon was dissolved in palladium during unselective, total hydrogenation. Additional studies of hydrogen content using in situ prompt gamma activation analysis, which allowed us to follow the hydrogen content of palladium during catalysis, indicated that unselective hydrogenation proceeds on hydrogen-saturated β-hydride, whereas selective hydrogenation was only possible after decoupling bulk properties from the surface events. Thus, the population of subsurface sites of palladium, by either hydrogen or carbon, governs the hydrogenation events on the surface.

A fundamental understanding of catalytic reactions requires a "bottom-up" approach using surface-science experiments and theoretical calculations to provide insights into surface dynamics and adsorbed species, their coverage, and possible reaction paths. For simple heterogeneous catalytic systems (such as ammonia synthesis and CO oxidation), the level of characterization approaches the point where rational insights into the design of the catalyst become feasible (1). Experimental studies have been aided by instrumental modifications that allow many surface-science techniques that typically are used under high-vacuum conditions to be used at modest pressures of reactants over the catalysts.

The presumed simplification of most studies is that the bulk of the catalyst, the part of the active sample below the surface, is "frozen" and can be neglected. Although heterogeneous catalytic conversion is a surface process, there is accumulating evidence, particularly from experiments applying in situ functional analysis, that the bulk and especially the subsurface region (the few layers below the surface) can play a key role in surface events. Reaction conditions (such as temperature and the ambient reactive gas) may not only reconstruct the top surface layer, but also may create added rows and valleys of atoms (2, 3) or even massively change the whole morphology of the catalytic particles (4). Atoms that are part of the catalytic feed can dissolve in metallic particles, and can change the electronic structure of the surface (5, 6), and dissolved species can even participate in the reaction (7). Here, we present a still relatively simple but industrially relevant case, alkyne hydrogenation on palladium, in which different subsurface species define which of the possible reaction paths dominates the overall reaction.

Many studies have addressed the question of how to selectively hydrogenate a certain functional group. A hydrocarbon with a carbon-carbon triple bond can be hydrogenated partially to the alkene or fully to the alkane. We have explored why palladium can selectively hydrogenate alkynes to alkenes, when Pd itself is usually even more active in hydrogenating the corresponding alkene to the alkane. The typical explanation (8) is that the difference in the heat of adsorption of the feed alkyne and of the partial hydrogenation product alkene forces the intermediate product alkene to desorb and become replaced by the incoming alkyne of the feed. However, 30 years ago, Al-Ammar et al. (9) demonstrated that, contrary to thermodynamic factors, ethylene could be adsorbed on a catalyst of Pd supported on silica while acetylene was present in the gas phase. This is possible because the surface of catalysts is usually heterogeneous and can have discrete sites that facilitate selective adsorption. Furthermore, many research groups have suggested that carbonaceous deposits formed during reaction might substantially affect selectivity [(10, 11) and references therein]. Alkyne hydrogenation usually goes through an
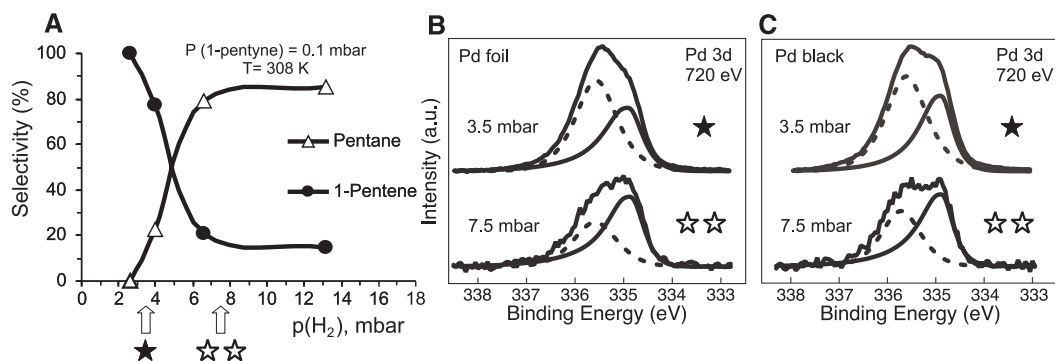
[1]Fritz-Haber-Institut der Max-Planck-Gesellschaft, Faradayweg 4-6, D-14195 Berlin, Germany. [2]Institute of Isotopes, Hungarian Academy of Sciences, Post Office Box 77, Budapest H-1525, Hungary. [3]WestCHEM, Department of Chemistry, University of Glasgow, Glasgow G128QQ, Scotland, UK.

*To whom correspondence should be addressed. E-mail: teschner@fhi-berlin.mpg.de

Fig. 1. Catalytic 1-pentyne gas-phase hydrogenation as a function of pH$_2$. (**A**) Selectivity for the two main reaction paths on Pd black; experiments were carried out in a closed-loop circulation setup. Hydrogenation selectivity is a strong function of pH$_2$. Solid and open stars mark pressures at which XPS experiments were carried out. P, pressure; T, temperature. (**B** and **C**) Corresponding Pd 3d$_{5/2}$ XP spectra recorded under hydrogenation conditions for Pd foil and black, respectively, using 720-eV excitation energy. The Pd component at 335 eV corresponds to bulk, metallic Pd, whereas the higher binding-energy peak (dashed line) represents the sum of adsorbate-induced surface core-level shift components and PdC. The reaction selectivity correlates with PdC: Selective hydrogenation occurs when the Pd peak is dominated by PdC, whereas total hydrogenation prevails on Pd containing much less C incorporated in the top few atomic layers. a.u., arbitrary units.